Article

Role of Calcium in the Proton Pump of Bacteriorhodopsin. Microwave Evidence for a Cation-Gated Mechanism

Robert R. Birge, Deshan S. K. Govender, K. Can Izgi, and Eric H. L. Tan

More About This Article

Additional resources and features associated with this article are available within the HTML version:

- Supporting Information
- Links to the 3 articles that cite this article, as of the time of this article download
- Access to high resolution figures
- Links to articles and content related to this article
- Copyright permission to reproduce figures and/or text from this article

View the Full Text HTML

Role of Calcium in the Proton Pump of Bacteriorhodopsin. Microwave Evidence for a Cation-Gated Mechanism

## Robert R. Birge,* Deshan S. K. Govender, K. Can Izgi, and Eric H. L. Tan

Department of Chemistry and W. M. Keck Center for Molecular Electronics, Syracuse University, 111 College Place, Syracuse, New York 13244-4100

Bacteriorhodopsin is the light-activated proton pump in the purple membrane of *Halobacterium salinarium*. One aspect of the proton pump mechanism that remains to be fully revealed is how back-translocation of the proton is eliminated despite the fact that gradients of 250 mV or more can exist in favor of reverse proton motion. This mechanistic component is examined with reference to the static and photodynamic resonances observed in the 1−40 GHz region of the microwave spectrum. The light-adapted form of bacteriorhodopsin displays strong microwave absorption with maxima near 8 and 25 GHz. We identify the origin of the microwave activity to protein-bound divalent cations by noting that (1) the ion-free blue membrane is microwave inactive, and (2) the microwave activity of the protein can be regenerated by adding calcium and/or magnesium to the protein. Initiation of the photocycle generates additional microwave activity in the low-frequency region of the spectrum. The **M** minus **bR** difference spectrum shows a single-cation resonance at 9.8 GHz. We assign this resonance to the release of a calcium ion from the chromophore-adjacent binding site into the proton channel. We conclude that a key biological role of the chromophore-adjacent calcium binding site is to provide a divalent cation gate that not only facilitates chromophore reprotonation but also prevents back-transfer of the proton during the latter stages of the photocycle.

I. Introduction

Bacteriorhodopsin is the light transducing protein in the photosynthetic purple membrane of *Halobacterium salinarium*.[1−13] This halophilic archaibacterium grows in salt marshes where the concentration of NaCl can exceed 4 M, roughly six times higher than seawater (∼0.6 M NaCl). The purple membrane, which contains the protein bacteriorhodopsin in a lipid matrix, is grown by the bacterium when the concentration of oxygen becomes too low to sustain growth via respiration (i.e. generation of ATP by oxidative phosphorylation). Upon the absorption of light, bacteriorhodopsin converts from a dark-adapted state containing a mixture of 13-cis and all-trans chromophores to a light-adapted state which contains only the all-trans chromophore. A view of the chromophore binding site showing some of the key amino acids residues[6] and the chromophore-adjacent calcium binding site[14] is shown in Figure 1. Subsequent absorption of light by the all-trans retinyl chromophore generates a photocycle which pumps protons across the membrane, with a net transport from the inside (cytoplasmic) surface to the outside (extracellular) surface of the membrane. The resulting pH gradient ($\Delta pH \approx 1$) generates a proton-motive force which is used by the bacterium to synthesize ATP from inorganic phosphate and ADP. The photocycle showing only selected intermediates along with their optical (λ_{max}) and conformational (chromophore geometry and protonation state) properties is summarized below:
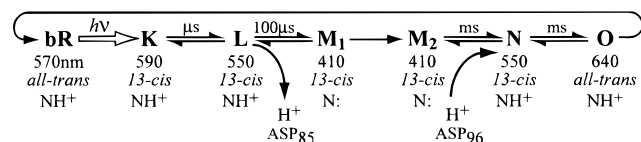
The mechanism of the proton pump of bacteriorhodopsin is a subject of fundamental importance to our understanding of biological structure and function. Recent studies have prompted renewed interest in the mechanism, due in part to the observation of nonlinear oscillatory behavior[11,12] as well as the ability of the protein to convert from a forward proton pump to a reverse chloride pump with the substitution of aspartate-85 (**ASP85**) by threonine.[15] One aspect of the proton pump mechanism that remains to be fully revealed is how the protein excludes back-translocation of the proton. The protein must pump a proton against a gradient which can reach $\Delta pH = 1.5$ (inside alkaline) and $\Delta\psi = 250$ mV.[16] The free energy required to pump a single proton across this gradient is approximately 6 kcal mol^{-1} (∼25 kJ mol^{-1}). The primary photochemical event stores 11.6 ± 3.5 kcal mol^{-1} (∼49 kJ mol^{-1}),[17] roughly twice the energy needed to overcome the barrier.[18,19] What is important here is the fact that during the photocycle, the proton pump mechanism must function against an uphill barrier. Microscopic reversibility considerations would naively suggest that the protein would permit back-transfer of the proton during the pumping process. In order to eliminate this reverse process, the mechanism must include a gating function that forces directionality on the pumping process. This important issue has been discussed recently from a variety of perspectives.[7−13,15]

The **M** state represents one of the most important intermediates within the photocycle. This intermediate is the only state in which the chromophore is deprotonated, and kinetic models of the photocycle suggest that there are two **M** states, **M1** and **M2**.[13,20−23] (We will refer to the **M** state, rather than to **M1** or **M2**, whenever both are involved or differentiation is not possible.) Relatively little is known about the molecular changes that take place during the **M1** → **M2** transition, but the fact that this reaction is unidirectional has important implications. It has been suggested that the **M1** → **M2** transition involves a nonreversible change in the protein conformation thereby providing a unidirectional proton pump.[13,21]

In this paper we present microwave spectra of bacteriorhodopsin and selected difference spectra of the protein as a function of photocycle and bound cations. We interpret our

---

* Author to whom correspondence should be addressed.
[⊗] Abstract published in *Advance ACS Abstracts,* May 1, 1996.

Proton Pump of Bacteriorhodopsin

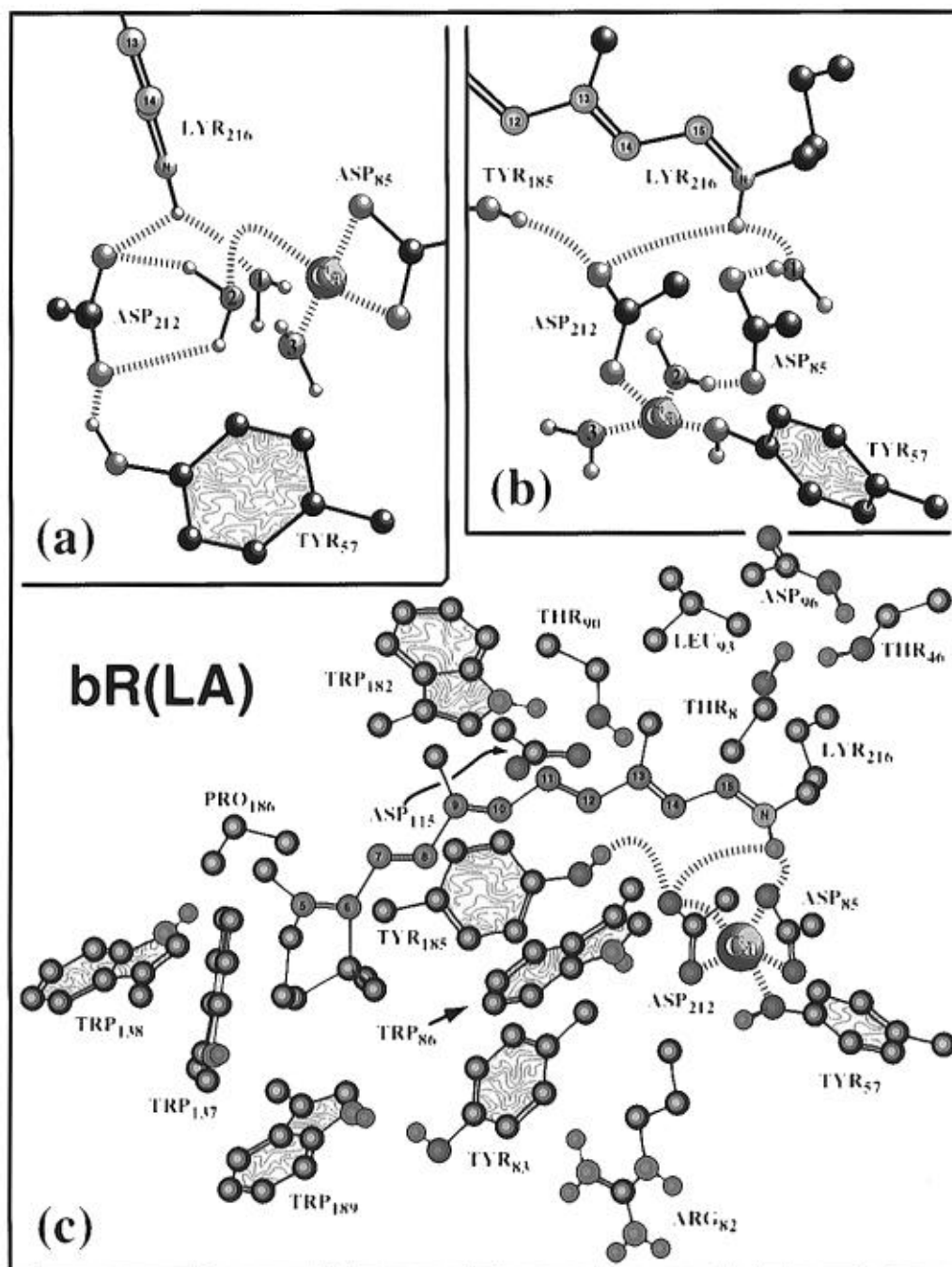*J. Phys. Chem., Vol. 100, No. 23, 1996* **9991**

Figure 1. (c) The chromophore and selected nearby amino acids that comprise the binding site of light-adapted bacteriorhodopsin. The structure is based on the diffraction data of Henderson and co-workers[6] and the nominal location of the calcium ion is based on spectroscopic and site-directed mutagenesis studies (see text). The chromophore is roughly in the plane of the page. The following amino acids are above the chromophore (**ASP85, ASP115, THR89, THR90, TRP137,** and **TYR83**) and the following amino acids are below the chromophore (**ASP212, PRO186, THR46, TRP182,** and **TYR185**). The remaining amino acids are roughly in the same plane as the chromophore. Key electrostatic and hydrogen bonding interactions are shown with dashed lines. The two residues in the upper-right-hand corner (**ASP96, LEU93,** and **THR46**) were moved vertically down to facilitate viewing. The two inserts (a and b) show the two minimum energy conformations of the near-chromophore calcium binding site (adapted from ref 14). [Color codes: carbon (black); nitrogen (blue); oxygen (red); hydrogen (green); chromophore carbon (orange). Only selected hydrogen atoms are shown for clarity.]

results to indicate that a calcium ion, released into the channel during the formation of the **M** state, acts as an electrostatic gate preventing back-transfer of the proton during the latter stages of the photocycle. The motion of the cation during the **M₁** → **M₂** transition may be a key element in the unidirectionality of this reaction.

II. Experimental Section

A. Protein Preparation and Purification. Purple membrane was isolated from a variant of the strain S9-P of *Halobacterium salinarium*, by using a modified protocol[14] based upon the procedures of Becher and Cassim[24] and Oesterhelt and Stoeckenius.[2] Strain S9-P was originally provided to us by John Spudich and is an enhanced overproducer of bacteriorhodopsin. Whereas the wild-type bacteria will only produce bacteriorhodopsin in its native form under certain physiological conditions,[2,25] i.e. under anaerobic conditions in the presence of steady illumination, strain S9-P will produce the purple membrane with high concentrations of dissolved oxygen and without illumination. It has been reported, however, that many strains produce

bacteriorhodopsin that has a high degree of heterogeneity. These different forms of the protein have been attributed to bacteriorhodopsin precursors: forms of the protein that are not fully maturated.[25-30] Production of these different forms of the protein, which include a 13 residue amino acid sequence attached to the glutamine that forms the amino terminus[26] and an aspartate residue attached to the carboxyl terminus (on SER-248), and various intermediate forms,[25,27,28] seems to be dependent upon culture conditions.[25] More specifically, different culture conditions allow different forms of the protein to accumulate, most of which are not fully maturated. Lorber and DeLucas, who studied bR production as a function of culture conditions, determined that the best method of obtaining a homogeneous protein preparation is one that involves the use of a fermenter with high rates of agitation and aeration (300 rpm and 3 L of air/min, respectively).[25] No illumination was required: in fact, their work included a study done in a glass fermenter surrounded by a bank of fluorescent tubes with lower agitation and aeration (50-100 rpm and 0.2 L/min) which produced mostly fully maturated bR, but traces of nonmaturated forms were also present. We have found that implementing the protocols suggested by these authors has greatly improved both our yields and the quality of bacteriorhodopsin isolated in our laboratory.[14] All of the samples used in this study were purified by using a sucrose density gradient ultracentrifugation. The latter was essential for producing reproducible microwave spectra, which suggests that carotenoids, or other species removed in the final purification step, may be responsible for spurious microwave signals.

Immediately prior to carrying out the microwave experiments, the PM suspension containing the protein and associated lipids was filtered by using a 5 μm Millipore filter followed by sonication at medium power for 10 min to reduce inhomogeneity. For convenience, we will refer to these filtered and sonicated aqueous suspensions as bacteriorhodopsin. All experiments were carried out on the light-adapted species generated by preirradiation of the sample for a minimum of 20 min with light from a slide projector (Kodak 4400 Projector) unless noted otherwise.

The blue membrane ($\lambda_{max} \approx 605$ nm) is a modified form of bacteriorhodopsin in which the divalent ions have been removed. We prepared the blue membrane by using the methods and procedures of Zhang et al.[31] Regeneration of the cation-specific purple membrane was accomplished by adding $CaCl_2$ or $MgCl_2$. Previous studies indicate that to a very good approximation, Ca^{2+} and Mg^{2+} ions occupy an identical chromophore adjacent divalent cation binding site (see discussion in ref 14).

B. Microwave Spectroscopy. We measured the microwave difference spectra by using time domain vectored network analysis (Figure 2). This technique determines the complex permittivity by measuring the phase and amplitude of the signal that is reflected from a coaxial probe immersed in the solution.[32] The principal instrumentation included an HP 8510C network analyzer controlled by an HP 9020B workstation. The frequency source was an HP 8340A synthesized sweeper coupled to an HP 8515A S parameter test set. All three instruments and the computer controller are manufactured by Hewlett-Packard Co., Palo Alto, CA.

The complex permittivity of the solution is measured following the procedures of Wei and Sridhar[32] with the following exceptions. First, the network analyzer is operated in time domain mode with a 125 ps time window centered at the probe tip. The use of time domain techniques decreases systematic and oscillatory errors due to signal reflections at the external connectors and within the S parameter test set. Second, all
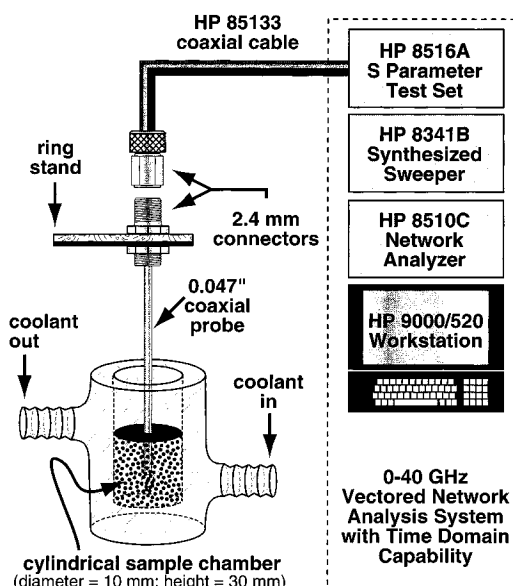

Figure 2. Schematic diagram of the apparatus used to measured microwave absorptivity spectra of bacteriorhodopsin in aqueous solution (network analysis instrumentation manufactured by Hewlett-Packard Co., Palo Alto, CA). Accuracy was improved by using time domain techniques with a 125 ps time window that minimizes error due to second-order reflections. The sample temperature was controlled by a thermostated refrigerated circulator bath (model RTE-8, Neslab Instruments Inc., Portsmouth, NH).

spectra were recorded as difference spectra, which removes a significant fraction of the systematic error due to fringe field capacitance and radiation loss. Unless specifically noted otherwise, the spectra are referenced to doubly distilled and deionized (dd&d) water. Third, and most important, three standard solutions of known complex permittivity are used to establish a quadratic response function which is used to calculate the properties of the unknown solution. A selection of 11 solvents (listed below) were used to assign the permittivity correction factors. The complex permittivities of the 11 solvents have been measured to high accuracy,[32-35] and the permittivity data can be fit by using a multiple relaxation dispersion model:

$$\epsilon_r(\nu) = \epsilon/\epsilon_0 = \epsilon' - i\epsilon'' = \epsilon_\infty + \sum_{k=1}^{n} \frac{\epsilon_k - \epsilon_{k+1}}{1 + i2\pi\nu\tau_k} \qquad (1)$$

where $\epsilon_r(\nu)$ is the relative complex permittivity at frequency ν, ϵ_k equals the relative permittivity of the kth dispersion region, $i = \sqrt{-1}$, τ_k is the relaxation time of the kth dispersion region, and n is the total number of dispersion regions included in the fit. We note that ϵ_{k+1} equals ϵ_∞ when $k = n$. The above model has been shown to provide a fit to the experimental data that agrees within experimental error, although three dispersion regions are often required (thus requiring seven variables). The above equation is easily evaluated in terms of the real and imaginary components of the permittivity. For a three region model, eq 1 reduces to

$$\epsilon'(\nu) = \epsilon_\infty + \frac{\epsilon_1 - \epsilon_2}{1 + (2\pi\nu\tau_1)^2} + \frac{\epsilon_2 - \epsilon_3}{1 + (2\pi\nu\tau_2)^2} + \frac{\epsilon_3 - \epsilon_\infty}{1 + (2\pi\nu\tau_3)^2}$$
$$(2a)$$

$$\epsilon''(\nu) = \frac{2\pi\nu\tau_1(\epsilon_1 - \epsilon_2)}{1 + (2\pi\nu\tau_1)^2} + \frac{2\pi\nu\tau_2(\epsilon_2 - \epsilon_3)}{1 + (2\pi\nu\tau_2)^2} + \frac{2\pi\nu\tau_3(\epsilon_3 - \epsilon_\infty)}{1 + (2\pi\nu\tau_3)^2}$$
$$(2b)$$

Proton Pump of Bacteriorhodopsin

J. Phys. Chem., Vol. 100, No. 23, 1996 **9993**

The appropriate values for the component terms required to evaluate eqs 1 and 2 are listed below on the basis of the convention:

$$\text{solvent name } [\{\epsilon_1, \tau_1\}, \{\epsilon_2, \tau_2\}, ..., \{\epsilon_n, \tau_n\}, \{\epsilon_\infty\}]),$$

where all of the relaxation times are in picoseconds and all data are for 25 °C. The data are as follows:[32−35]

acetone   [{21.2, 3.3}, {1.9}]

water   [{77.97, 8.32}, {6.18, 1.02}, {4.49}]

formamide
[{108.8, 37.3}, {7.08, 1.16}, {4.48}]

N,N-dimethylformamide
[{37.24, 10.4}, {4.38, 0.76}, {2.94}]

N,N-dimethylacetamide
[{38.43, 16.0}, {4.10, 1.33}, {3.04}]

N-methylformamide
[{183.3, 128}, {6.13, 7.93}, {4.60, 0.78}, {3.20}]

methanol
[{32.50, 51.5}, {5.91, 7.09}, {4.90, 1.12}, {2.79}]

ethanol
[{24.32, 163}, {4.49, 8.97}, {3.82, 1.81}, {2.69}]

1-propanol
[{20.43, 329}, {3.74, 15.1}, {3.20, 2.40}, {2.44}]

2-propanol
[{19.40, 359}, {3.47, 14.5}, {3.04, 1.96}, {2.42}]

We also used 1,4-dioxane [{2.2}] and air [{1}] as standards for which $\epsilon'' = 0$ and $\epsilon' = \epsilon_\infty$. As an example of interpreting the above grouped listings we note that the explicit variable assignments for methanol are as follows: $\epsilon_1 = 32.50$, $\tau_1 = 51.5$ ps, $\epsilon_2 = 5.91$, $\tau_2 = 7.09$ ps, $\epsilon_3 = 4.90$, $\tau_3 = 1.12$ ps, $\epsilon_\infty = 2.79$.

The first step in making a measurement is to carry out a one-port three-step calibration following standard procedures.[32] Air and mercury are used to assign the open and closed (shorted) reference standards. Subsequently, three solvent standards (e.g. 2-propanol, methanol, and water) are used to provide an initial set of error correcting polynomials. The electrical delay and the phase are normalized and the sample is measured. On the basis of the results of the initial sample measurement, three new solvent standards are chosen so that one standard exhibits absorptivities slightly above the sample, the second standard is as close as possible to the sample, and third is slightly below the sample with respect to absorptivity across the 5−35 GHz region. The three new solvent standards are then used to define a new set of error correcting polynomials, and the sample is remeasured. Normally, the new measurement is in good agreement with the previous measurement and the process is not repeated. Occasionally, the initial and subsequent measurements disagree and a third series is required. By using the above techniques, the average error for the real and imaginary components of the permittivity for the three probes tested were as follows: 0.047 in. probe (1.7% for ϵ'; 4.0% for ϵ''), 0.085 in. probe (1.9%; 4.2%), and HP 85075A (3.1%; 2.8%). The corresponding worst case errors were as follows: 0.047 in. (3.0%; 5.7%), 0.085 in. (3.7%; 5.8%), and HP 85075A (5.8%; 7.1%). All of the spectra reported in this paper were obtained by using the 0.047 in. coaxial probe. At least 128 spectra were

averaged in each case, and all of the key experiments were carried out on a variety of different samples prepared by using different purification methods to verify that sample history did not play a significant role in defining the spectra features. We note that a sucrose density purification of the protein is essential to reproducibility.

The propagation constant is a complex quantity given by

$$\gamma = \alpha + i\beta \qquad (3)$$

where α is the attenuation constant and β is the phase constant. The wavelength (λ) and the velocity (u) of the signal in the solution is determined by the phase constant [$\lambda = u/\nu = 2\pi/\beta$]. The attenuation constant determines the absorptivity of the solution, which provides the most relevant interface between experiment and theory (see section III). The electric field strength is attenuated within the sample on the basis of the following relationship:

$$E_1 = E_0 \exp[-\alpha L] \qquad (4)$$

$$\alpha(\nu) = \frac{\nu\pi\sqrt{2\epsilon'}}{c_0}(\sqrt{1 + (\epsilon''/\epsilon')^2} - 1)^{1/2} \qquad (5)$$

where E_0 is the initial electric field amplitude, E_1 is the electric field amplitude after passing through a length, L, of the sample, $\alpha(\nu)$ is the attenuation constant at frequency ν, and c_0 is the speed of light in vacuum. In other words, after traveling a distance of $1/\alpha$, the electric field amplitude is attenuated to $1/e$ times its initial value. By convention, the attenuation constant is listed in units of dB/cm:

$$\alpha(\text{dB/cm}) = 20 \log_{10}(e) \, \alpha(1/\text{cm}) \approx$$
$$1.287237 \times \nu(\text{GHz})\sqrt{\epsilon'}(\sqrt{1 + (\epsilon''/\epsilon')^2} - 1)^{1/2} \quad (6)$$

which is derived by noting that dB $= 20 \log_{10}(R)$, where R is the amplitude or voltage ratio. In the present case, the ratio is replaced by the actual value of α in units of cm^{-1}, with the latter units carried through for reference. The above units can be converted to molar absorptivity, a_ϵ, provided the concentration of the solute is known:

$$a_\epsilon(\text{M}^{-1} \text{ cm}^{-1}) = \frac{0.05\alpha(\text{dB/cm})}{C(\text{M})} \approx$$
$$0.0643618\frac{\nu(\text{GHz})\sqrt{\epsilon'}}{C(\text{M})}(\sqrt{1 + (\epsilon''/\epsilon')^2} - 1)^{1/2} \quad (7)$$

where C is the concentration of the absorbing species in mol/L (M). All of the protein-based microwave spectra reported here were collected on 65 μM solutions, and for these cases, 1 dB/cm is equivalent to a molar absorptivity of 769 M^{-1} cm^{-1}.

An error analysis of the attenuation constant carried out by using pure solvent samples indicates that the errors in absorptivity are less than 1 dB/cm in the region 5−35 GHz, but increase dramatically above 35 GHz. The worst case error in the 35−40 GHz region approaches ±5 dB/cm, which precludes the measurement of reliable spectra in this region, even with pure samples. A reliance on difference spectra improves the worst case error in the 35−40 GHz region to values closer to ±2 dB/cm. An additional source of error for protein samples is associated with inhomogeneity of the sample. As shown in Figure 3, the volume that is addressed by a coaxial probe immersed in aqueous solution is dependent upon the frequency, and at the higher frequencies used in this study (35−40 GHz), a relatively small volume at the end of the tip is absorbing 99%
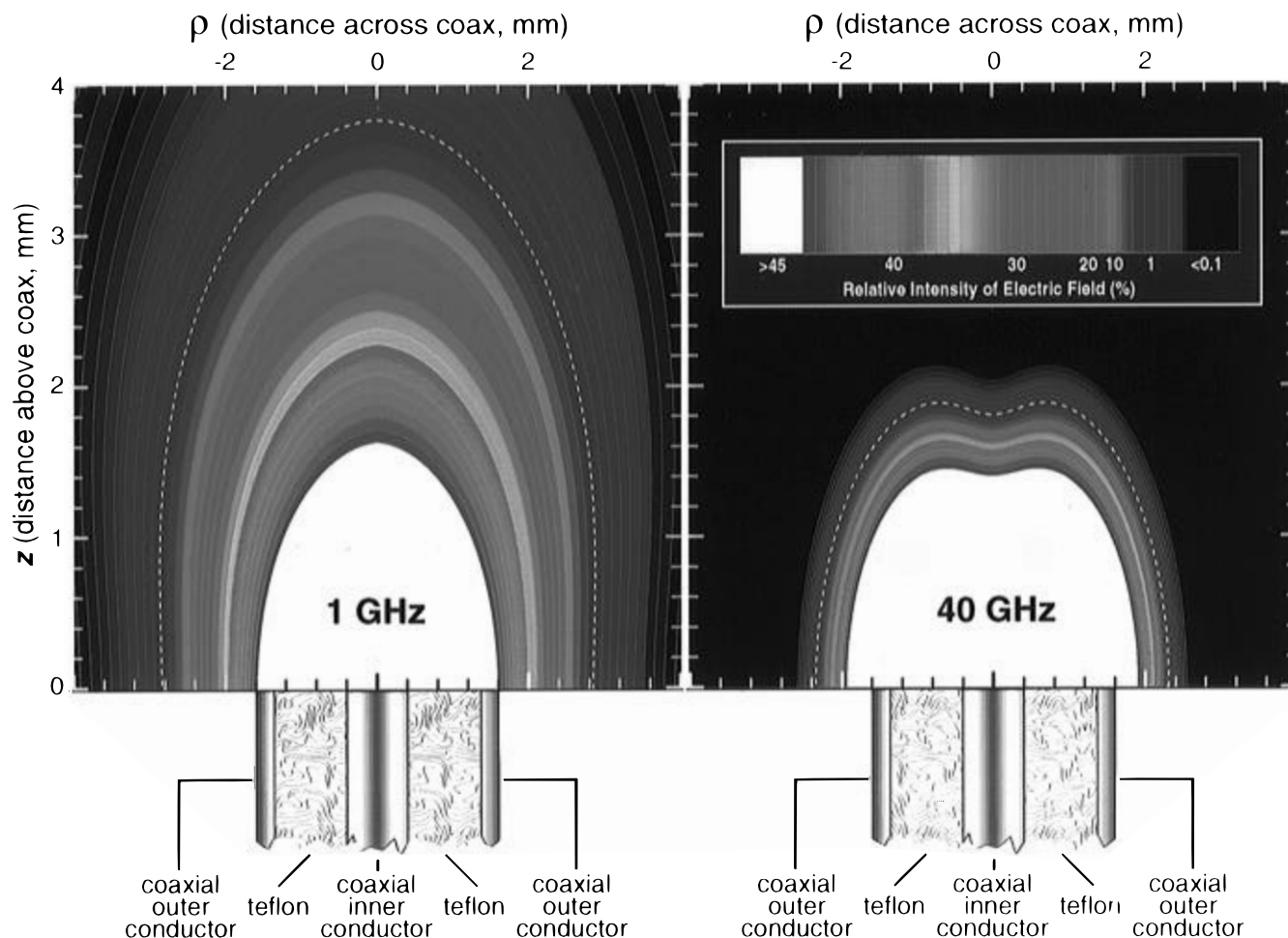
Figure 3. Power absorption contours for the 0.047 in. coaxial probe immersed in water at 1 (left) and 40 GHz (right). The thick dotted lines represent the contours within which 99% of the radiation is absorbed. Thus, the measurement of the microwave absorptivity in the 1−40 GHz region addresses a volume element that contracts at higher frequencies thus requiring a highly homogeneous sample to avoid artifacts. The absorption contours were calculated by using the equivalent magnetic current source methods of Swicord and Davis.[36]

of the energy.[36] Thus, the presence of large protein fragments or an aggregation of smaller protein fragments can produce a frequency-dependent response due to inhomogeneous populations of the fragments in the solution. In addition, fringe field effects become much more important at the higher frequencies. We minimized the above-mentioned sources of error by filtering and sonicating all of our solutions prior to measurement. The use of water as a solvent also introduces an important source of error into difference spectra in the 35−40 GHz region due to the high absorptivity of the solvent in this region. The intrinsic noise floor of the network analyzer is approximately 180 dB, but the absorptivity of water is 176 dB/cm at 35 GHz and increases to 198 dB/cm at 40 GHz. To a first approximation, difference spectra measured in water at frequencies above 35 GHz are not possible. By using averaging and careful phase control, spectra features can be observed above 35 GHz, but difference spectra above 35 GHz must be considered of only qualitative significance. Fortunately, all of the key spectral features relevant to the present study are at frequencies below 35 GHz.

III. Theory

Theoretical treatments of microwave spectroscopy have traditionally concentrated on the analysis of gas-phase rotational and vibrational spectra.[37] Solution-phase microwave absorption has normally been analyzed in terms of hindered rotational events often using multiple dispersion relaxation models as

previously described (eqs 1−5).[32−35] None of the above approaches provides useful insight regarding the resonances observed in the present study of bacteriorhodopsin (see below). We therefore investigated the alternative models described below. These models, despite their relative simplicity, provide useful insights into the molecular events responsible for the observed microwave spectra.

A. Channeled-Ion Theory. Channeled-ion theory represents a simple model describing the frequency-dependent microwave activity of a charged species restricted along a channel of a fixed length. The potential energy of the ion inside the channel is assumed to be negligible and outside of the channel, infinite. Channeled-ion theory is a modification of the free electron model with explicit inclusion of the effect of Boltzmann population on the oscillator strength and the use of effective masses and channel lengths to compensate for finite-sized charged species.

The wave function of the charged species is given by

$$\psi(n,x) = (2/L_{\text{eff}})^{1/2} \sin\left(\frac{n\pi x}{L_{\text{eff}}}\right) \tag{8}$$

where x is the coordinate of the major axis of the channel of effective length, L_{eff} ($0 \leq x \leq L_{\text{eff}}$) and n (or m) is the quantum number for motion along the major axis ($n,m = 1, 2, 3, ...$). As discussed in section IV.B.1 below, L_{eff} is more appropriately viewed as a quantization length. The charged species can be a

Proton Pump of Bacteriorhodopsin

J. Phys. Chem., Vol. 100, No. 23, 1996 **9995**

distributed (spatially large) entity, but the oscillation of the particle in response to the applied electromagnetic field can be many times smaller than L_{eff}. The stationary state energy of the charged species as a function of the quantum state is given by

$$E(n) = \frac{n^2 h^2}{8 M_{eff} L_{eff}^2} \qquad (9)$$

where h is Planck's constant and M_{eff} is the effective mass of the charged species. The transition length of the $m \rightarrow n$ transition is given by

$$\langle \psi(n,x)|x|\psi(m,x)\rangle = \begin{cases} \dfrac{-8 L_{eff} mn}{\pi(n-\mathrm{m})^2 (m+n)^2} & (n-m \text{ odd}) \\ 0 & (n-m \text{ even}) \end{cases} \qquad (10)$$

and the oscillator strength of the $m \rightarrow n$ transition is given by

$$f_{mn} = \frac{8\pi^2 M_{eff}}{3h^2} P_{mn}(E(n) - E(m))|\langle\psi(n,x)|x|\psi(m,x)\rangle|^2 \qquad (11a)$$

where P_{mn} is the Boltzmann population difference between the nth and mth states

$$P_{mn} = \frac{\exp[-E(m)/kT] - \exp[-E(n)/kT]}{\displaystyle\sum_{i=1}^{\infty}\exp[-E(i)/kT]} \qquad (11b)$$

Equation 11b assumes that all of the levels are in thermal equilibrium, which is a reasonable assumption for the experimental conditions utilized in our experiments. We approximated the partition function in the denominator of eq 11b by carrying out the summation over the lowest 9000 levels (an additional 3000 levels produced a change of less than one part-per-million in the partition function).

The microwave spectra are simulated by using Gaussian profiles to represent the individual transitions:

$$A_{rel}(\nu) = \sum_{n=m+1}^{\infty}\sum_{m=1}^{\infty} \frac{1}{\Delta\nu_{fwhm}\sqrt{\pi}}\left\{f_{mn}\exp\left[\frac{-(\nu-\nu_{mn})^2}{\Delta\nu_{fwhm}^2}\right]\right\} \quad (12)$$

where $A_{rel}(\nu)$ is the relative absorbance at frequency ν associated with the summation over all $n \leftarrow m$ transitions, f_{mn} is the oscillator strength (eq 11a) and ν_{mn} is the frequency of the $n \leftarrow m$ transition $\{\nu_{mn} = [E(n) - E(m)]/h\}$. The full-width at half-maximum of the individual Gaussian profiles, $\Delta\nu_{fwhm}$, is assumed identical for all transitions ($\Delta\nu_{fwhm} = 0.14$ GHz). The results are not sensitive to $\Delta\nu_{fwhm}$ values in the range 0.1–0.5 GHz because the density of allowed transitions overwhelms any fine structure that might be observed in the $A_{rel}(\nu)$ profile. Values of $\Delta\nu_{fwhm}$ above 0.5 GHz start to broaden the total band profile. The summations are approximated by limiting the ensemble to 9000 levels, an upper limit which includes all states relevant for the present set of spectral simulations.

B. Superionic Conduction Theory. Superionic conductors are ionic materials that have high electrical conductivities due to the motion of ions which can be thermally activated from a stable position in the lattice to occupy a region within the lattice where nearly unrestricted motion is possible.[38] The frequency-dependent reflectance of a superionic conductor is given by

$$R(\omega) = \frac{[n'(\omega) - 1]^2 + [n''(\omega)]^2}{[n'(\omega) + 1]^2 + [n''(\omega)]^2} \qquad (13)$$

where $n'(\omega)$ is the real refractive index, $n''(\omega)$ is the imaginary refractive index, and ω is the angular frequency of the radiation ($\omega = 2\pi\nu$). The frequency-dependent refractive indices are related to the dielectric constants of the medium by the following relationships:

$$n'^2(\omega) = \frac{1}{2}[(\epsilon'^2(\omega) + \epsilon''^2(\omega))^{1/2} + \epsilon'(\omega)] \qquad (14a)$$

$$n''^2(\omega) = \frac{1}{2}[(\epsilon'^2(\omega) + \epsilon''^2(\omega))^{1/2} - \epsilon'(\omega)] \qquad (14b)$$

where ϵ' is the real dielectric constant and ϵ'' is the imaginary dielectric constant:

$$\epsilon'(\omega) = \epsilon'(\omega_{high}) - \frac{\omega_p^2}{(\omega^2 + \omega_{damp}^2)} \qquad (15a)$$

$$\epsilon''(\omega) = \frac{\omega_{damp}\,\omega_p^2}{\omega(\omega^2 + \omega_{damp}^2)} \qquad (15b)$$

where ω_p is the collisionless ion resonance frequency, $\epsilon'(\omega_{high})$ is the real dielectric constant at the high-frequency end of the microwave region, and ω_{damp} is the ion damping frequency. The collisionless ion resonance frequency is a function of the charge and mass of the ion as well as the volume in which the ion is confined:

$$\omega_p = \left[\frac{q^2}{M_{eff}V_{eff}\epsilon_0\epsilon'(\omega_{high})}\right]^{1/2} \qquad (16)$$

where q is the charge on the ion (or species), M_{eff} is the effective mass of the ion (or species), V_{eff} is the effective volume that "confines" the ion, and ϵ_0 is the permittivity of vacuum. The damping frequency is given by

$$\omega_{damp} = \frac{2\pi kT}{h}\exp[-E_{barrier}/kT] \qquad (17)$$

where $E_{barrier}$ is the energy barrier height. The kinetic energy of the ion must exceed this barrier to enter the conducting channel (or volumetric region defined by V_{eff}). Implicit in this simple theory is the assumption that the ion is trapped when it has an energy below $E_{barrier}$ and is fully mobile within the effective volume when it has an energy above $E_{barrier}$. The effective volume is a poorly defined variable, due in part to the fact that it is defined in terms of a plasma density function. For example, semiconductor-directed models replace V_{eff} by $1/N_{mobile}$, where N_{mobile} is the number density of the mobile ions. The latter is calculated based on Boltzmann statistics: $N_{mobile} = N_0 \exp[-E_{barrier}/kT]$, where N_0 is the total ion density. In this formulation, all of the mobile ions must have access to the entire lattice, an assumption that is not justified for ions confined to a protein channel or cavity. However, the theory transfers best to protein systems when we relate the effective volume to the protein cavity volume, V_0, by the following relationship:

$$V_0 = V_{eff}\exp[-E_{barrier}/kT] \qquad (18)$$

Equation 18 retains the plasma-like dynamics inherent in superionic conduction theory by adjusting the true volume to a larger effective volume.

9996 *J. Phys. Chem., Vol. 100, No. 23, 1996*

Birge et al.

The reflectivity can now be defined by using the following relationship:

$$R(\omega) = [1 + 4\epsilon'(\omega_{high}) + 4\Gamma_1 +$$
$$\Gamma_1{}^2 - 2\Gamma_2 - 2\sqrt{2(1+\Gamma_1)^2(2\epsilon'(\omega_{high}) + \Gamma_1 - \Gamma_2)]}\Big/$$
$$[1 - 4\,\epsilon'(\omega_{high}) + \Gamma_1{}^2 + 2\,\Gamma_2] \quad (19)$$

where Γ_1 and Γ_2 are dimensionless constants given by

$$\Gamma_1 =$$
$$\sqrt{\frac{\epsilon'(\omega_{high})^2\,\omega_{damp}{}^2\,\omega^2 + \epsilon'(\omega_{high})^2\,\omega^2 - 2\,\epsilon'(\omega_{high})\,\omega^2\,\omega_p{}^2 + \omega_p{}^4}{\omega_{damp}{}^2\,\omega^2 + \omega^4}}$$
$$(20a)$$

$$\Gamma_2 = \frac{2\omega_p{}^2}{\omega_{damp}{}^2 + \omega^2} \quad (20b)$$

The absorptivity (optical density), A, is now given by

$$A(\omega) = \log_{10}\left(\frac{1}{|R(\omega)|}\right) \quad (21)$$

C. Molecular Orbital Theory. Ground-state calculations on the binding site were carried out by using MNDO/PM3 all-valence electron semiempirical molecular orbital procedures.[39-42] We used the PM3 Hamiltonian because it is parameterized for magnesium.[41] Parameters for calcium are not available, and thus all of our simulations of metal ions in the binding site were carried out by using magnesium to represent the divalent cation. This substitution should have no significant impact on our basic conclusions, because both calcium and magnesium are bivalent and appear to be identical in terms of impact on the optical spectroscopic properties of bacteriorhodopsin.[14] [We note, however, interesting differences in the microwave spectra (see below).] Excited-state calculations were carried out by using INDO-PSDCI and MNDO-PSDCI molecular orbital theory.[14,43-45] The CI basis set included all singles and all doubles from the π-electron system of the chromophore. All excited-state calculations simulating the divalent cation binding site were based on the PM3 Hamiltonian, which is not parameterized for excited state calculations. We adjusted the σ- and π-electron mobilities on the basis of the recommendations of Zerner (m_σ = 1.25, m_π = 0.585).[46] These modifications allow us to use ground-state parameterization with reasonable success in simulating the one-photon properties of the protonated Schiff-base chromophores.[14]

IV. Results and Discussion

A. Molecular Origins of the Microwave Spectra. Microwave spectra of bacteriorhodopsin in aqueous solution are shown in Figure 4. Both light-adapted and dark-adapted bacteriorhodopsin exhibit a very strong microwave absorption spectrum with maxima at about 8 and 25 GHz. Analysis of the spectra shown in Figure 4b indicates that the origin of the microwave activity of bacteriorhodopsin is due to protein-bound divalent cations. The cation-free blue membrane ($\lambda_{max} \approx 605$ nm) exhibits no observable microwave activity (Figure 4b). The spectrum of the blue membrane can be described to a first approximation as due to the displacement of water by a non-microwave active material (e.g. toluene). When $CaCl_2$ (or $MgCl_2$) is added to the blue membrane in solution, the Ca^{2+} (or Mg^{2+}) ions diffuse into the protein interior and restore the purple color and photochemical activity of the protein ($\lambda_{max} \approx$
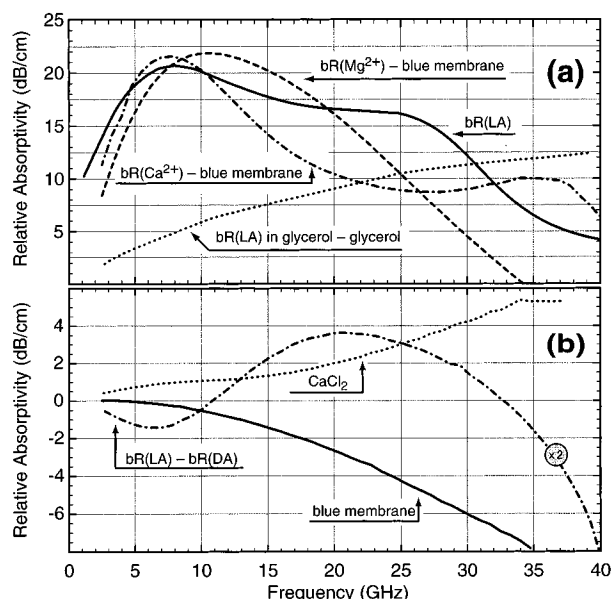

Figure 4. The microwave absorptivity of light-adapted bacteriorhodopsin, **bR(LA)** in (a), in doubly distilled and deionized (dd&d) water (pH = 7; 25 °C) is compared with the absorptivity of the blue membrane (b), $CaCl_2$ (b) and regenerated **bR** (a) under comparable conditions. All spectra are difference spectra, with the reference being dd&d water (pH = 7; 25 °C) unless noted explicitly. The **bR(LA)** − **bR(DA)** difference spectrum has been multiplied by two to facilitate viewing. The solute concentration was 65 μM in all cases and the solutions were sonicated for 30 min to achieve optimal homogeneity. The spectrum of the blue membrane plus calcium was corrected for solution bound ions by using an ion selective analyzer (Model EA 940 Orion ion analyzer, Cambridge, MA) along with a double junction reference electrode to measure free calcium ion concentrations and by subtracting the appropriate free ion spectrum.

570 nm).[14,31,47-54] These ions restore the microwave activity of the protein (Figure 4a). There are two possible origins for the microwave activity. The first possibility is that the cations modify the structure of the protein, and some unidentified structure within the protein becomes microwave active. The second possibility is that the cations are directly responsible for the absorption. The spectra shown in Figure 4a provide strong support for the latter model. First we note that magnesium and calcium regenerated **bR** produce significantly different microwave spectra (Figure 4a), but virtually identical optical spectra (see discussion in ref 14). Second, we find that changes in solvent environment (see below) have a dramatic effect on the spectrum, which suggests that the mass of the solvent is important in determining the frequency. This observation would follow from hydration effects on the ion as examined in more detail below. Third, theoretical simulations of the spectra indicate that large amplitude motion of a charged species is responsible (see below), and a bound cation provides the most likely candidate. We conclude from the above observations that the principal source of the microwave absorptivity of bacteriorhodopsin in water is due to the cations that are intrinsically present in the native protein.

Microwave spectra of bacteriorhodopsin in glycerol (not shown) do not display peak resonances below 40 GHz, but rather exhibit a broad-band absorptivity slowly rising toward higher frequency. Thus, water is also involved, either directly or indirectly, in adjusting the frequency or presence of cation-based resonances. Neutron diffraction studies indicate that there are about four tightly bound water molecules in the binding site.[55] Furthermore, we can eliminate the possibility that free calcium in the (protein external) water solution is responsible for the major peaks observed in the spectra. A 65 μM solution of $CaCl_2$

Proton Pump of Bacteriorhodopsin

J. Phys. Chem., Vol. 100, No. 23, 1996 **9997**

in water does not produce low-frequency resonances with the same intensity or location as those observed in the protein (see Figure 4b). Furthermore, the spectrum of the blue membrane plus calcium was corrected for solution-bound ions by using an ion-selective analyzer (Model EA 940 Orion ion analyzer, Cambridge, MA) along with a double-junction reference electrode to measure free calcium ion concentration and by subtracting the appropriate free ion spectrum. (A similar experimental correction for the magnesium spectrum was not possible, due to the unavailability of a magnesium-selective electrode. We assumed identical free Mg^{2+} concentrations as observed for the Ca^{2+} data in making our free Mg^{2+} spectral correction.) We conclude with confidence that the protein, metal cations, and water must all be present to generate the strong microwave resonances observed in Figure 4a.

Previous studies have demonstrated that there are two high-affinity calcium binding sites within the protein.[14,31,51,52,54,56,57] The first site has a much higher affinity for calcium than does the second site,[54] and it has been shown that at roughly equimolar ratios of Ca(II) to blue membrane, the cation is preferentially bound to the first site.[52] Previous studies have shown that the first site is not responsible for the blue to purple transition (which correlates with occupation of the second site).[14,52] Site-directed mutagenesis studies of bacteriorhodopsin suggest that the first and second sites are within interaction distance with one another and with the charged residues in the retinal binding site.[31] Two-photon studies find evidence for only a single calcium binding site near to the chromophore, although electrostatic maps suggest that there are regions near the chromophore that are invisible to cation occupation with respect to optical spectroscopy.[14] When we prepared a 2:1 mixture of blue membrane and Ca(II), we observed virtually no activity below 20 GHz and a broad unstructured increase in the microwave absorptivity above 20 GHz. Thus, the highest affinity site is microwave active, but has a peak resonance above 35−40 GHz. Titration of the blue membrane with additional Ca(II) generates rapid growth of the 25 GHz band as well as 8−10 GHz band. We were unable to observe a correlation between the relative intensity of these two peaks and the second vs lower affinity sites. Thus, the second high-affinity site may also produce a resonance above 35−40 GHz. However, we cannot exclude the possibility that the band at 25 GHz in **bR-(LA)** is associated with the second high-affinity site. Theoretical simulations of the spectra by using channeled-ion and superionic resonance models (see below) suggest that the band at 8−10 GHz is due to hydrated cations loosely bound within the proton conducting channel or weakly bound calcium ions on or near the protein surface.

Analysis of the integrated oscillator strength of the microwave spectrum suggests that 6−8 cations are contributing to the observed spectrum below 40 GHz. Previous studies indicate there are between 3−5 cations bound per protein.[47,50] The studies of Mitra and Stroud indicate that there are in fact six binding sites, but that there are only three cations dynamically occupying these six sites.[50] Our observation that as many as eight cations may be spectroscopically active may indicate some cations are bound very weakly, suggesting the possibility of nonspecific binding of cations to the protein surface.[58,59] In addition, some hydrated cations may drift into the proton channel and become microwave active (see discussion below).

There is a small difference between light-adapted and dark-adapted spectra as shown in the **bR(LA)** minus **bR(DA)** spectrum shown in Figure 4b (note that the difference spectrum has been multiplied by two to facilitate viewing). We attribute this difference spectrum to a small change in the cation
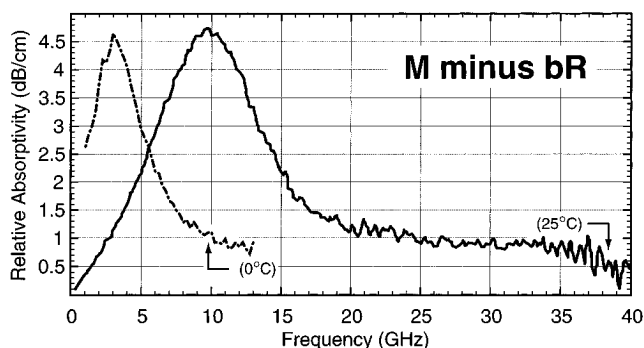

Figure 5. The **M** minus **bR** difference spectra of 65 μM light-adapted bacteriorhodopsin at 0 °C (dd&d water, pH = 7) and 25 °C (dd&d water; 1,3-diaminopropane (10%; w/w); pH = 9.5) (see text).

environment associated with the two states of the protein. The key difference between these two protein states is that in dark-adapted bacteriorhodopsin, the chromophore is in a roughly 50:50 equilibrium of 13-cis and 13-trans species. In light-adapted bacteriorhodopsin, all of the chromophores are photochemically converted to the all-trans conformation (see Figure 1). This change in chromophore geometry will likely affect the near-chromophore calcium binding site, but the spectra suggest that light adaptation generates small changes in some of the other cation binding sites.

B. Microwave Spectra of the M State. The **M** state ($\lambda_{max} \approx 410$ nm) is a key intermediate in the photocycle of light-adapted bacteriorhodopsin. The blue shift of the absorption band is due to deprotonation of the retinyl Schiff base. It has long been known that the decay kinetics of the **M** state consist of a slow and a fast component. More recent kinetic studies have provided strong evidence in support of a dual **M** state, and more interestingly, the fact that the two **M** states, M_1 and M_2, are coupled such that only the forward reaction ($M_1 \rightarrow M_2$) is observed.[13,20−23] During the $L \rightarrow M_1$ transition, the imine proton on the chromophore is transferred to ASP_{85} and a proton is subsequently ejected from the proton channel into the extracellular medium. During the $M_2 \rightarrow N$ transition, ASP_{96} transfers a proton to the chromophore and a proton is subsequently taken up at the cytoplasmic surface. Relatively little is known about the molecular changes that take place during the $M_1 \rightarrow M_2$ transition, but the fact that this reaction is unidirectional has important implications. It has been suggested that the $M_1 \rightarrow M_2$ transition involves a nonreversible change in the protein conformation thereby providing a unidirectional proton pump.[13,21] We will refer to the **M** state, rather than to M_1 or M_2, whenever both are involved or differentiation is not possible.

We trapped the **M** state by using 10% 1,3-diaminopropane and high pH (9.5) and measured the **M** minus **bR** difference spectrum at 25 °C (Figure 5). The steady-state concentration of the **M** state was increased to >50% by using a filtered (500 < λ < 650 nm) 100 W halogen lamp. Although the mechanism is not well understood, it is known that 1,3-diaminopropane and high pH significantly increase the lifetime of the **M** intermediate. We verified that the spectral features were invariant to both 1,3-diaminopropane concentration and pH by carrying out a series of experiments as a function of additive concentration and pH. We also measured the **M** minus **bR** difference spectrum in deionized water at 0 °C, a temperature that provides sufficient stabilization of the **M** state to permit observation (Figure 5). The solution does not freeze at 0 °C for a protein concentration of 65 μM. The ambient temperature spectrum is very reproducible (±5%; 3−35 GHz), but the 0 °C spectrum is variable (>20%) and exhibits a variance that is a function of

sample history with respect to both intensity and frequency. [The effect of history is most easily explained in terms of changes in E_{barrier} (eq 17) as discussed below (section IV.B.2).]

The oscillator strength of the ambient temperature **M** minus **bR** difference spectrum is observed via integration to fall between 7×10^{-6} and 7×10^{-5}, a broad range which is associated with two experimental uncertainties. The lowest value is based on the assumption that we have full conversion to the **M** state and that all **M** states remain microwave active over the full time scale of our experiment. We estimate that we are likely producing less than 80% **M**, and thus this value is invariably an underestimate. More complicated is the assumption that the **M** state exhibits a temporally invariant activity. While this is a logical assumption, the time-resolve dielectric loss experiments of McIntosh and Boucher suggest the possibility that the spectrum may change with time as the **M** state relaxes.[60] This must remain an open question because a direct correspondence of the time-resolved dielectric loss measurements (which were carried out at a fixed frequency) and our experiments (which provide frequency dispersion but are averaged over many minutes) may not be measuring the same properties of the system. Indeed, McIntosh and Boucher suggest that they are observing charge transport during the photocycle. In summary, further work will be required to resolve this issue, but we cannot exclude the possibility that the spectrum is more intense during the initial formation of the **M** state and that after dynamic relaxation, the spectrum either decreases in intensity or shifts to higher energy. We estimate an upper limit of the oscillator strength to be approximately 7×10^{-5}, which leads to the following range for the experimental value:

$$7 \times 10^{-6} < f_{\text{exp}}(\mathbf{M} - \mathbf{bR}) < 7 \times 10^{-5} \qquad (22)$$

Identification of the molecular origin of the 9.8 GHz resonance in the **M** minus **bR** difference spectrum is important to our analysis of the proton-pumping mechanism. To investigate possible molecular mechanisms, we simulated the spectra by using three models. The theoretical simulations are compared to experiment in Figure 6 and discussed below. For the purposes of visual comparison, the simulations shown in Figure 6 were normalized so that the calculated maxima were coincident with the observed spectrum.

B.1. Channeled-Ion Model. A charged species of mass M_{eff} is assumed to oscillate along a one-dimensional (or pseudo one-dimensional) channel of length L_{eff} (see section III.A). The position of the resonance at 9.8 GHz can be accommodated for any M_{eff} and L_{eff} obeying the following relationship:

$$M_{\text{eff}} \times L_{\text{eff}}^2 \approx 2.185 \times 10^{-45} \text{ kg m}^2 = 1.316 \times 10^6 \text{ amu Å}^2 \qquad (23)$$

While, the normalized theoretical spectrum shown in Figure 6a is generated for any model that satisfies the above relationship, the intensity of the resonance is proportional to L_{eff}. An approximate upper limit to L_{eff} of 48 Å can be assumed on the basis of the transmembrane dimension of the protein. This length would require an effective mass of 571 amu and yields a calculated oscillator strength of 2.5×10^{-4}. The calculated value of the oscillator strength is almost an order of magnitude larger than the upper limit for the experimental value. A more realistic value of $L_{\text{eff}} = 24$ Å requires $M_{\text{eff}} = 2284$ amu and predicts an oscillator strength of 6.4×10^{-5}. This calculated value for the oscillator strength is within the predicted experi-
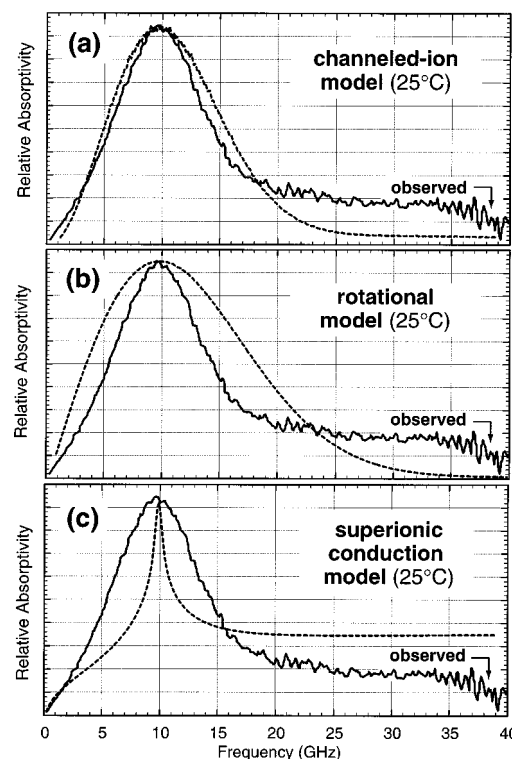

Figure 6. Three theoretical models of the ambient temperature **M** minus **bR** difference spectrum are compared to the observed spectrum (25 °C, from Figure 5) (see text).

mental range (eq 22). We conclude on the basis of the channeled-ion model that the effective mass must be roughly 2000 amu or larger.

At this point it is useful to consider the proton-conducting intermembrane segment of the protein as a possible candidate for the channel. The model shown in Figure 7 is based on the model proposed by Henderson and co-workers on the basis of their diffraction data[6] and supported by spectroscopic and site-specific mutagenesis studies.[7−10,13,14] The tilted cylinder which encloses this region of the protein has a length of ~26 Å and a diameter of ~5 Å leading to a total volume of ~500 Å³ (Figure 7). The length is in good agreement with the above choice of $L_{\text{eff}} = 24$ Å, but the volume raises important issues with respect to the effective mass, $M_{\text{eff}} = 2284$ amu, that is calculated based on the chosen value of L_{eff}. If we were to fill the entire volume of the cylinder shown in Figure 7 with water at a standard density of 1000 kg/m³, we would only have a total mass of ~300 amu. While the effective mass value must be treated with qualitative rather than quantitative significance, the large difference between the above two mass values points to an important conclusion. Either the channel-ion model is inadequate to rationalize the observed **M** minus **bR** microwave difference spectrum, or the mass that is moving in responsive to the electric field is significantly larger than the mass enclosed within the proton channel. An alternative view is that the calcium ion is strongly coupled to one or more amino acid residues which are attached to the α helices (**C** and/or **G**; Figure 7), and segments of the α helices are strongly coupled to the large amplitude motion of the ion. We will conclude that the latter is not only possible, but highly likely. Thus, while the charged species can be identified as calcium (or magnesium), the motion of calcium is strongly associated with one or more amino acid residues within the channel.

The large amplitude motion of the charged species can be analyzed in terms of the amplitude expectation value by using
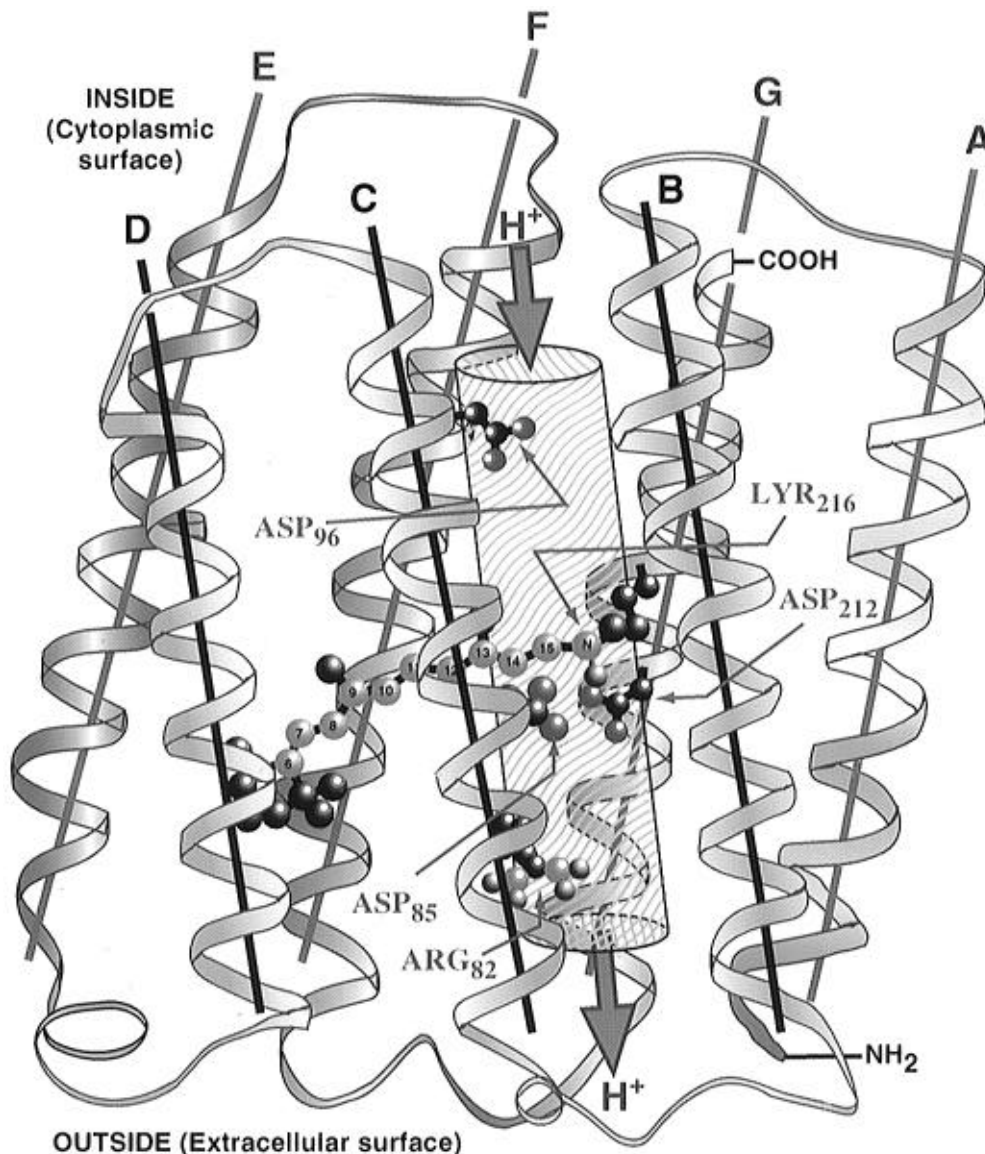
Proton Pump of Bacteriorhodopsin

J. Phys. Chem., Vol. 100, No. 23, 1996 **9999**

Figure 7. The proton channel in bacteriorhodopsin is shown with reference to the seven α helical segments (gold ribbons in front, blue ribbons in back) and selected amino acid residues that participate in the proton pumping process. The shaded gray cylinder (volume ≈ 500 Å³) has a length of about 26 Å and a diameter of about 5 Å and delineates the approximate volumetric region of the proton channel.

the following semiclassical equation:

$$\Delta x = \left(\frac{h}{2\nu_{res}M_{eff}}\right)^{1/2} \approx$$
$$1.01 \text{ Å } (\nu_{res} = 9.8 \text{ GHz}, M_{eff} = 2000 \text{ amu}) \quad (24)$$

which indicates for an effective mass of about 2000 amu an expectation value of ~1 Å of motion of the charged species. This positional shift is significantly larger than is encountered by atoms during nominal vibrational modes, but is many times smaller than L_{eff}. This result suggests that we should view L_{eff} in terms of a quantization length rather than a region of zero potential for the charged species.

B.2. Rotational Model. A majority of molecular resonances in the microwave region involve rotational transitions, but such transitions are invariably observed in the gas phase. Molecular collisions that characterize solution environments invariably shift the corresponding gas-phase rotational transitions to higher frequencies, and invariably eliminate the type of localized resonances observed in Figure 5. Nevertheless, the possibility that the protein might accommodate a free or slightly hindered

internal rotation needs to be considered. We simulated a rotational spectrum by assuming a near symmetric top and using the standard equations to calculate the transitions and relative intensities.[37] The best fit spectrum is shown in Figure 6b for the following rotational constants ($A = 3.75$ MHz, $B = 3.72$ MHz, $C = 2.01$ MHz). Although we investigated a number of molecular models involving internal rotations, no realistic models involving a cation and water-generated rotational constants within 1 order of magnitude of the above values. More complicated models including hindered internal rotations were also tested,[37] but no physically realistic model was found. There are two additional issues that preclude enthusiasm for a rotational model. First, the shape of the observed band is contrary to that expected for a rotational band. Regardless of model, all of our simulated rotational spectra were much broader than the observed spectrum (Figure 6b). Inhomogeneous broadening would likely increase the full-width at half-maximum, making the correspondence between rotational models and our observed spectrum even worse. Second, the observation that the spectrum shifts dramatically to lower frequency at reduced temperature (Figure 5) is difficult to accommodate on the basis of an internal rotational model. We

10000 *J. Phys. Chem., Vol. 100, No. 23, 1996*

Birge et al.

conclude that internal rotations are unlikely to contribute to the observed **M** minus **bR** difference spectrum.

B.3. Superionic Conduction Model. Superionic conductors are materials that have ions normally trapped in some site, but which through thermal motion, can occupy regions in which relatively free motion is possible.[38] The theory described in section III.C is routinely used to examine the interaction of radiation with inorganic crystalline solids, ion-doped glasses, and ion-doped polymers. The mobile ions in these systems are normally cations. Recent studies have indicated that superionic conduction theory can be used to model the frequency-dependent dielectric loss exhibited by cations incorporated into organic channels such at polymeric crown ethers.[61]

A common characteristic of superionic conductors is the tendency for the microwave absorptivity to display a relatively sharp band at lower frequency and a nearly flat attenuation at high frequencies. The **M** minus **bR** difference spectrum shows the key characteristics of an inhomogeneously broadened superionic conductor.[61] The simulation shown in Figure 6c was generated by assuming the following parameters: $\omega_p = 400$ GHz; $E_{barrier} = 8$ kJ/mol; $\epsilon'(\omega_{high}) = 1.5$; $q = 1$ e. (The prediction that the spectroscopic charged species has a charge of 1 versus 2 is important and is discussed below.) These values require that the product of effective mass times volume equal:

$$M_{eff} \times V_{eff} \approx 1.21 \times 10^{-50} \text{ kg m}^3 = 7.28 \times 10^6 \text{ amu Å}^3$$

Restating this equation in terms of the protein cavity volume requires the use of eq 18 and assignment of $E_{barrier}$ (= 8 kJ/mol). At 25 °C, $\exp[E_{barrier}/kT]$ equals 25.3 and we get

$$M_{eff} \times V_0 \approx 4.78 \times 10^{-48} \text{ kg m}^3 = 2.88 \times 10^5 \text{ amu Å}^3 \quad (25)$$

If we make the assumption that the charged species is moving about within the proton channel, an approximate upper limit to the volume of this channel is $V_0 = 500$ Å^3 (Figure 8), which means the effective mass of the charged species is ~580 amu. A more realistic volume range would be closer to $100-200$ Å^3 leading to $M_{eff} \approx 1400-2800$ amu. When we compare these results with those obtained from the channeled-ion model we find reasonable agreement. The most realistic values for the channeled−ion model give $L_{eff} = 24$ Å, $M_{eff} = 2284$ amu and $f = 6.4 \times 10^{-5}$ (eq 23 and section B.1). Thus, the effective mass is predicted to be roughly 2000 amu. Finally, we note that the spectrum cannot be fit within the constraints of realistic V_0 by assuming that the ionic species has a net charge of 2 proton units. The charge is squared in the calculation of ω_p (eq 16), and hence superionic conduction theory is rather sensitive to the charge.

Both the superionic conduction model and the channeled-ion model can simulate the motion of a charged species along a channel, although the two models approach the event from different perspectives and formalisms. To the extent that both models make similar predictions about the effective mass is encouraging. Indeed, there is a general agreement on the size of the cavity occupied by the charged species. If we assume that the cavity is cylindrical as shown in Figure 7, then reconciliation of eqs 23 and 25 predicts a diameter of ~3 Å, a value somewhat smaller than that of the cylinder shown in Figure 7. An alternative volume element is the large (water-filled) cavity predicted by the models of Sampogna and Honig.[62] This cavity lies between **ASP**$_{85}$ and **ASP**$_{212}$ and extends toward **ARG**$_{82}$ and appears to include the ionic portion of the latter residue (see Figure 2, ref 62). The cylinder shown in Figure 7 intercepts this volume element, and thus the selection of one
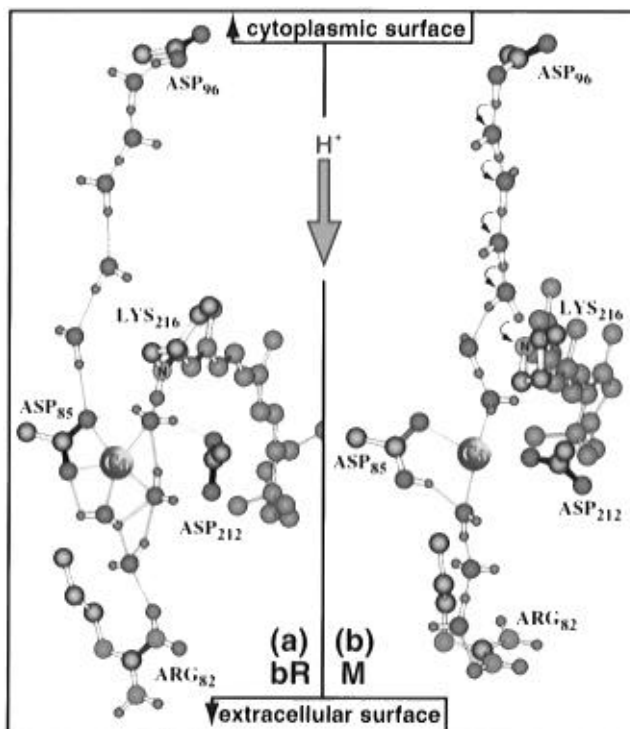

Figure 8. Molecular models of the **bR** (a) and **M** (b) states of bacteriorhodopsin showing the chromophore, selected amino acids and the near-chromophore calcium binding site. Some of the water molecules as well as the **ASP**$_{96}$ and **ARG**$_{82}$ residues have been rotated slightly to facilitate viewing. Two water molecules coordinating with calcium above and below the plane are not shown. Directions toward the cytoplasmic and extracellular surfaces and the proton pumping vector are indicated. Calcium is tightly bound in **bR**, weakly bound and microwave active ($\nu_{max} = 9.8$ GHz) in **M**. The reprotonation pathway from **ASP**$_{96}$ to the chromophore nitrogen is indicated by arrows (b) and represents the key event that forms the **N** intermediate. [Color codes: carbon (black); nitrogen (blue); oxygen (red); hydrogen (green); chromophore carbon (orange). Only selected hydrogen atoms are shown for clarity.]

volume vs the other may be irrelevant. However, reconciliation of the channeled-ion model and the superionic conduction model favors the cylindrical cavity shown in Figure 7.

B.4. Molecular Models. If we eliminate the possibility that the **M** minus **bR** difference spectrum is due to rotational degrees of freedom within the protein (see section B.2), the models presented above suggest that the spectrum is associated with the translational motion or oscillation of a large charged species ($M_{eff} \approx 2000$) within a fairly large cavity with a length of about 25 Å. We summarize our conclusions below:

Observation 1. The microwave spectra of **bR** are due to divalent metal cations with important contributions from water molecules.

Observation 2. The microwave active species in the **M** minus **bR** difference spectrum has an effective mass of ~2000 amu and undergoes large amplitude motion perpendicular to the membrane normal.

Observation 3. The microwave active species in the **M** minus **bR** difference spectrum has a charge of +1, which indicates that a negative counterion is intimately associated with the divalent metal cation.

Observation 4. The metal cation associated with the **M** minus **bR** difference spectrum must experience a significant change in environment that shifts the microwave activity down in frequency by a factor of at least 4.

Thus, we conclude that the **M** minus **bR** difference spectrum is due to a calcium ion released into the channel, or for which

Proton Pump of Bacteriorhodopsin

J. Phys. Chem., Vol. 100, No. 23, 1996 **10001**

the environment has changed such that its translational motion is coupled into the chain of water molecules that form a portion of the proton conducting channel. The large effective mass is due to strong electrostatic coupling of the metal ion translation with a single negatively charged amino acid, which is covalently attached to the α helix. Current models of the chromophore-adjacent calcium binding in **bR**[14,31,51,52,54] coupled with current models of the **M** state[7,10,13,63−75] and reconciliation of the above four observations regarding the microwave spectra lead to the models shown in Figure 8. These models were refined by using MNDO/PM3 molecular orbital theory and the systematic minimization of 11 water molecules (two water molecules coordinating with calcium above and below the plane are not shown).

The model of the chromophore-adjacent calcium binding site of **bR** shown in Figure 8a is a simplification of the more detailed models shown in parts a and b of Figure 1. Additional stabilization of the calcium ion in **bR** is provided by **TYR85** and/or **TYR185**. The formation of the blue-shifted **M** intermediate results in deprotonation of the retinyl Schiff base with the transfer of a proton to **ASP85**. This process is likely mediated by water.[55,75−78] The protonation of **ASP85** destabilizes the calcium binding site and forces the calcium ion to interact strongly with **ASP212**, the only negatively charged amino acid in close proximity. Additional stabilization of the calcium ion in **M** is provided by **TYR85** (not shown). We conclude that the increased translational degree of freedom of calcium is responsible for the 9.8 GHz microwave signal that is observed in the **M** minus **bR** difference spectrum (Figure 5). The prediction based on superionic-conduction theory that the net charge of the charged species is one (not two) is indicative of strong coupling between Ca^{2+} and **ASP212**. This coupling adds to the effective mass by coupling the mass of portions of the **G** transmembrane helical segment (Figure 7) to that of the hydrated calcium ion. This coupling provides a qualitative explanation of the unusually large effective mass predicted by the spectral simulations (sections B.1 and B.3). In the following section we examine the relevance of these models to the mechanism of proton pumping in bacteriorhodopsin.

C. The Role of Calcium in the Proton Pump. On the basis of the molecular models of **bR** and **M** shown in Figure 8, we conclude that the hydrated calcium ion carries out two important functions in the proton pumping mechanism. First, it occupies a key position within the proton channel and the resulting electrostatic field prevents back-translocation of the proton. Second, the calcium ion draws the "water wire" that formerly coupled **ASP96** to **ASP85** in **bR** toward the chromophore in **M**. This facilitates reprotonation of the chromophore during the **M** → **N** transition. We examine the above two issues in more detail below.

The protein must pump a proton against a gradient which can reach ΔpH = 1.5 (inside alkaline) and Δψ = 250 mV.[16] Microscopic reversibility considerations would naively suggest that the protein would permit back-transfer of the proton during the pumping process. In order to eliminate this reverse process, the mechanism must include a gating function that forces directionality on the pumping process. The calcium cation occupies a central position within the proton conducting channel, and upon the formation of the **M** state, the strong electrostatic coupling of Ca^{2+} with **ASP212** produces a net positive charge located roughly in the center of the proton conducting channel. On the basis of a simple electrostatic model of the gate, back-translocation of the proton through the channel will experience a barrier of

$$E_{\text{barrier}}(H^+) \approx \frac{e^2}{4\pi\epsilon_0\epsilon_r r_{\text{channel}}} = \frac{332 \text{ kcal}}{\text{mol}} \frac{1}{\epsilon_r r_{\text{channel}}(\text{Å})} \quad (26)$$

where ϵ_r is the relative permittivity (dielectric constant) of the medium and r_{channel} is the radius of the proton channel. If the radius of the channel were greater than 3 Å, then it would be appropriate to assume one water molecule can shield the proton from the charged species and ϵ_r would equal ∼80. At distances below 3 Å, the proton must be transferred via a mechanism that is not water assisted, and $\epsilon_r \approx 1$. The radius of the channel is somewhere between 1.5 Å (see discussion in section 3.B.3) to 2.5 Å (Figure 7), which means $\epsilon_r \approx 1$ and the calculated energy barrier equals ∼130 kcal/mol (∼550 kJ/mol). A more sophisticated analysis based on PM3 semiempirical molecular orbital theory and hydronium ion translocation predicts a smaller barrier of ∼32 kcal/mol (∼134 kJ/mol). Nevertheless, the latter barrier is capable of withstanding a transmembrane potential of >1 V, four times larger than the nominal upper limit encountered *in vivo*.[16] The above analysis, however, neglects contraction and motion of the transmembrane α helices, and we anticipate that at potentials approaching 1 V, our assumptions of a fixed protein backbone would no longer be valid. It is sufficient for the purposes of the present discussion to state with confidence that the electrostatic potential of the Ca^{2+}:**ASP212**:nH_2O monovalent species precludes back transfer of the proton via the proton conducting channel shown in Figure 7 under the nominal transmembrane potentials encountered both *in vivo* and *in vitro*.

As noted above, our simulations predict that the metal cation serves an additional role in the proton pumping mechanism. As shown in Figure 8, a water molecule within the proton wire coupling **ASP96** to the chromophore binding site shifts toward the imine nitrogen in **M** (presumably **M₂**) and provides a direct pathway for the proton on **ASP96** to transfer to the Schiff-base nitrogen (labeled "**N**" in Figure 8). The arrows shown in Figure 8b predict the reprotonation mechanism responsible for forming the **N** intermediate. This model is in good agreement with the proton water wire model originally proposed by Nagle.[79] It has now been well-established that water plays a key role in transferring a proton from **ASP96** to the Schiff base of retinal.[80] Our cation-based model of the process is also supported by the recent studies and conclusions of Brown et al.[81] These investigators replaced **ASP212** and **ARG82** with neutral residues (**ASN212** and **GLN82**). The lifetime of the **M** intermediate in the double mutant was dramatically reduced, but the proton wire was still formed permitting proton translocation from **ASP96** to the chromophore. These observations provide indirect support for the importance of the calcium ion in drawing the proton wire. Our model may also provide a useful perspective on why trivalent metal ions stabilize the **M** state. Ariki and Lanyi have shown that substitution of the divalent metal cations with trivalent lanthanide ions increases significantly the **M** state lifetime.[56] A number of investigators have shown that the substitution of the divalent metal cations with trivalent cations increases the **M** state lifetime by factors of 10−100.[47,56,82−86] The additional positive charge on the metal ion will have a significant effect on the structure of the binding site, and would likely shift the position of the proton wire, or due to extensive hydration of the trivalent cation, destroy the structure of the proton wire entirely. The above studies underscore the importance of the metal cation in the reprotonation step. Although it is known that monovalent cations can restore the purple color of bacteriorhodopsin, detailed kinetic studies of the photocycle have not been carried out for monovalent cation regenerated **bR** (see discussion in refs 14, 50, 87, and 88). If our models
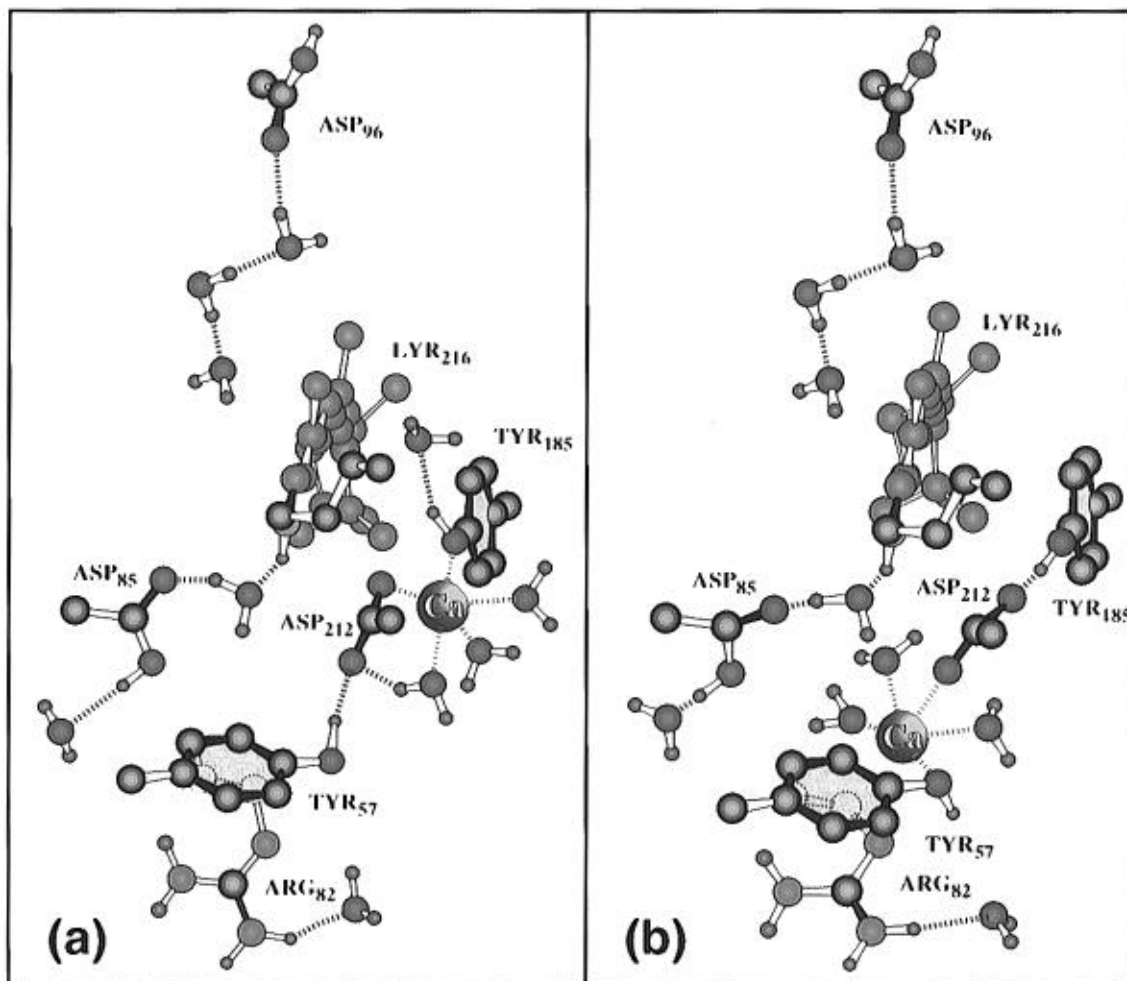
Figure 9. Two alternative molecular models of the **O** state based on MNDO/PM3 simulations. The model shown in a is the lowest energy conformation with the calcium ion stabilized by ASP_{212}, TYR_{185}, and three water molecules. The model shown in b is the kinetically favored conformation with the calcium ion stabilized by ASP_{212}, TYR_{57}, and three water molecules. Some models of the photocycle predict two **O** states (see discussion in ref 10). Our calculations suggest that the initial **O** state (**O_1**) is b and the subsequent **O** state (**O_2**) is a. Some of the water molecules as well as the ARG_{82} residue have been rotated or shifted slightly to facilitate viewing. Vertical orientation of the structure and color codes are identical to those shown in Figure 8.

are correct, however, the gating mechanism could still function efficiently with monovalent cations provided two monovalent cations were bound within the near-chromophore divalent cation binding site. We note that our model of this site includes two minimum energy conformations (Figures 1a and 1b), and both can be populated simultaneously with monovalent cations. A similar situation exists for our models of the **O** state, where we find two potential binding sites for the cation with comparable energy (see next paragraph).

In closing, we note that the metal cation must be "reset" during the $O \rightarrow bR$ step. Two models of the **O** state are shown in Figure 9. The first model (Figure 9a) is the minimum energy model in which the metal cation is stabilized by ASP_{212}, TYR_{185} and three water molecules. The second model (Figure 9b), in which the metal cation is stabilized by ASP_{212}, TYR_{57}, and three water molecules, is slightly higher in energy than the first model, but is kinetically favored. In other words, on the basis of our models of **M** and **N**, direct motion of the calcium cation into the position shown in Figure 9b is likely. Some models of the proton pump mechanism include two **O** states (see discussion in ref 10). If two states are present and involve different calcium binding sites, we suggest that O_1 is Figure 9b and O_2 is Figure 9a. The kinetic studies of Varo and Lanyi based on electronic difference spectra do not predict two **O** states.[22,23,89] However, the two models are predicted by MNDO/PSDCI molecular orbital theory[14] to have nearly identical Franck−Condon maxima

for the lowest-lying allowed ($^1B_u{}^{*+}$-like) state, and thus it would be unlikely that the spectroscopic consequences on the electronic absorption spectra of these two states could be observed. It is likely that two additional water molecules are providing enhanced stabilization to the Ca^{2+}:ASP_{212}:TYR_X:$3H_2O$ complexes, but our simulations provide no definitive conformational assignment for the two additional water molecules, and they are not shown. Whether we choose the energetically favored (Figure 9a) or kinetically favored (Figure 9b) model for **O**, the $O \rightarrow bR$ reaction will require two molecular events: deprotonation of ASP_{85} and motion of the calcium ion into a position to stabilize both ASP_{85} and ASP_{212}. The lifetime of the **O** state will therefore be dependent in part on the size and mass of the positively charged cation. To investigate the kinetics of this process in more detail, we have replaced the metal cations with large monovalent organic tetraalkyl amines and divalent bolaform amines.[88] We find that the half-life of the **O** state is linearly proportional to the mass of the divalent bolaform cations (Figure 10). We do not suggest that these results provide direct support for our models of the **O** state (Figure 9). The results do provide evidence that the divalent cation occupying the chromophore-adjacent binding site shifts to a different but specific binding site in the **O** state. We also noted an effect on the **M** state kinetics. The decay of the **M** intermediate is biphasic, composed of a fast and slow component. While the formation and slow decay are similar for all of the analog
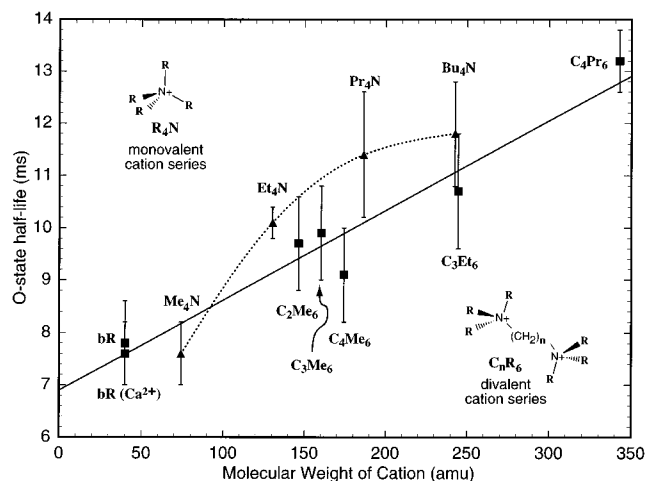
Proton Pump of Bacteriorhodopsin

J. Phys. Chem., Vol. 100, No. 23, 1996 **10003**

Figure 10. The half-life of the **O** intermediate is plotted as a function of the molecular weight of the organic cation. The kinetic data for the divalent bolaform amines are linear with respect to molecular weight within experimental error (straight line shows a least-squares fit). The monovalent tetraalkylamines must be bound in pairs to simulate the divalent metal cation and the kinetics display a quadratic dependence on molecular weight.

proteins, the fast decay is slower for the larger cations.[88] These results suggest that the fast decay involves cation movement. These results, when analyzed in combination, provide additional support for the general features of our model of the proton pump, and the importance of the chromophore-adjacent cation in mediating the process.

We conclude that a key biological role of the near-chromophore calcium binding site is to provide a divalent cation gate that not only facilitates chromophore reprotonation but also prevents back-transfer of the proton during the latter stages of the photocycle.

References and Notes

(1) Oesterhelt, D.; Stoeckenius, W. *Nature (London), New Biol.* **1971**, *233*, 149−152.

(2) Oesterhelt, D.; Stoeckenius, W. *Methods Enzymol.* **1974**, *31*, 667−678.

(3) Oesterhelt, D.; Schuhmann, L. *FEBS (Fed. Eur. Biochem. Soc.) Lett.* **1974**, *44*, 262−265.

(4) Stoeckenius, W.; Bogomolni, R. *Annu. Rev. Biochem.* **1982**, *52*, 587−616.

(5) Birge, R. R. *Biochim. Biophys. Acta* **1990**, *1016*, 293−327.

(6) Henderson, R.; Baldwin, J. M.; Ceska, T. A.; Zemlin, F.; Beckmann, E.; Downing, K. H. *J. Mol. Biol.* **1990**, *213*, 899−929.

(7) Mathies, R. A.; Lin, S. W.; Ames, J. B.; Pollard, W. T. *Annu. Rev. Biophys. Biophys. Chem.* **1991**, *20*, 491−518.

(8) Oesterhelt, D.; Tittor, J.; Bamberg, E. *J. Bioenerg. Biomembr.* **1992**, *24*, 181−191.

(9) El-Sayed, M. A. *Acc. Chem. Res.* **1992**, *25*, 279−286.

(10) Ebrey, T. G. Light energy transduction in bacteriorhodopsin. In *Thermodynamics of membrane receptors and channels*; Jackson, M. B., Ed.; CRC Press: Boca Raton, 1993; pp 353−387.

(11) Tributsch, H.; Bogomolni, R. A. *Chem. Phys. Lett.* **1994**, *227*, 74−78.

(12) Birge, R. R. *Nature* **1994**, *371*, 659−660.

(13) Lanyi, J. K. *Nature* **1995**, *375*, 461−463.

(14) Stuart, J. A.; Vought, B. W.; Zhang, C. F.; Birge, R. R. *Biospectroscopy* **1995**, *1*, 9−28.

(15) Sasaki, J.; Brown, L. S.; Chon, Y.-S.; Kandori, H.; Maeda, A.; Needleman, R.; Lanyi, J. K. *Science* **1995**, *269*, 73−75.

(16) Lanyi, J. K. *Microbiol. Rev.* **1978**, *42*, 682−712.

(17) Birge, R. R.; Cooper, T. M.; Lawrence, A. F.; Masthay, M. B.; Zhang, C. F.; Zidovetzki, R. *J. Am. Chem. Soc.* **1991**, *113*, 4327−4328.

(18) Recent photoacoustic calorimetric studies suggest a much higher energy storage in the primary event.[19] This difference should be expected. Low-temperature photocalorimetry measures the enthalpy of a thermally trapped species; in contrast, ambient temperature photoacoustic calorimetry measures the energy of a transient species assuming that all excess energy has been transferred to the solvent. Transient protein states with sub-microsecond lifetimes can store kinetic energy localized within the protein framework that is not transferred fully to the solvent environment during the time scale of the measurement. The extent to which this excess energy is available to subsequent intermediates remains to be determined.

(19) Rohr, M.; Gärtner, W.; Schweitzer, G.; Holzwarth, A. R.; Braslavsky, S. E. *J. Phys. Chem.* **1992**, *96*, 6055−6061.

(20) Lanyi, J. K. *J. Bioenerg. Biomembr.* **1992**, *24*, 169.

(21) Lanyi, J. K. *Adv. Chem.* **1994**, *240*, 491−510.

(22) Varo, G.; Lanyi, J. K. *Biochemistry* **1991**, *30*, 5016−5022.

(23) Varo, G.; Lanyi, J. K. *Biochemistry* **1991**, *30*, 5008.

(24) Becher, B. M.; Cassim, J. Y. *Prep. Biochem.* **1975**, *5*, 161−178.

(25) Lorber, B.; DeLucas, L. J. *FEBS Lett.* **1990**, *261*, 14−18.

(26) Seehra, J. S.; Khorana, H. G. *J. Biol. Chem.* **1984**, *259*, 4187−4193.

(27) Wölfer, U.; Dencher, N. A.; Büldt, G.; Wrede, P. *Eur. J. Biochem.* **1988**, *174*, 51−57.

(28) Ross, P. E.; Helgerson, S. L.; Miercke, L. J. W.; Dratz, E. A. *Biochim. Biophys. Acta* **1989**, *991*, 134−140.

(29) Miercke, L. J. W.; Ross, P. E.; Stroud, R. M.; Dratz, E. A. *J. Biol. Chem.* **1989**, *264*, 7531−7535.

(30) Betlach, M.; Pfeifer, F.; Friedman, J.; Boyer, H. W. *Proc. Natl. Acad. Sci. U.S.A.* **1983**, *80*, 1416−1420.

(31) Zhang, Y. N.; El-Sayed, M. A.; Bonet, M. L.; Lanyi, J. K.; Chang, M.; Ni, B.; Needleman, R. *Proc. Natl. Acad. Sci. U.S.A.* **1993**, *90*, 1445−1449.

(32) Wei, Y. Z.; Sridhar, S. *Rev. Sci. Instrum.* **1989**, *60*, 3041−3046.

(33) Barthel, J. K.; Bachhuber, K.; Buchner, R.; Gill, J. B.; Kleebauer, M. *Chem. Phys. Lett.* **1990**, *167*, 62−66.

(34) Barthel, J.; Bachhuber, K.; Buchner, R.; Gill, J. B.; Kleebauer, M. *Chem. Phys. Lett.* **1990**, *165*, 369−373.

(35) Misra, D. M.; Chabbra, B. R.; Epstein, M.; Mirotznik, M.; Foster, K. R. *IEEE Trans. Microwave Theory Tech.* **1990**, *38*, 8−14.

(36) Swicord, M. L.; Davis, C. C. *IEEE Trans. Microwave Theory Tech.* **1981**, *11*, 1202−1208.

(37) Townes, C. H.; Schawlow, A. L. *Microwave spectroscopy*; Dover: New York, 1975.

(38) *Physics of Superionic Conductors*; Salamon, M. B., Ed.; Springer-Verlag: New York, 1979.

(39) Dewar, M. J. S.; Thiel, W. *J. Am. Chem. Soc.* **1977**, *99*, 4899.

(40) Dewar, M. J. S.; Zoebisch, E. G.; Healy, E. F.; Stewart, J. J. P. *J. Am. Chem. Soc.* **1985**, *107*, 3902−3909.

(41) Stewart, J. J. P. *J. Comput. Chem.* **1989**, *10*, 221−245.

(42) Thiel, W. *Tetrahedron* **1988**, *44*, 7393.

(43) Tallent, J. R.; Hyde, E. Q.; Findsen, L. A.; Fox, G. C.; Birge, R. R. *J. Am. Chem. Soc.* **1992**, *114*, 1581−1592.

(44) Tallent, J. R.; Birge, J. R.; Zhang, C. F.; Wenderholm, E.; Birge, R. R. *Photochem. Photobiol.* **1992**, *56*, 935−952.

(45) Birge, R. R.; Gross, R. B.; Masthay, M. B.; Stuart, J. A.; Tallent, J. R.; Zhang, C. F. *Mol. Cryst. Liq. Cryst. Sci. Technol. Sec. B. Nonlinear Optics* **1992**, *3*, 133−147.

(46) Zerner, M. C. Semiempirical molecular orbital methods. In *Reviews in Computational Chemistry*; Lipkowitz, K. B., Boyd, D. B., Eds.; VCH Publishers: New York, 1990; pp 313−365.

(47) Chang, C. H.; Chen, J. G.; Govindjee, R.; Ebrey, T. *Proc. Natl. Acad. Sci. U.S.A.* **1985**, *82*, 396−400.

(48) Chang, C.-H.; Jonas, R.; Melchiore, S.; Govindhee, R.; Ebrey, T. G. *Biophys. J.* **1986**, *49*, 731−739.

(49) Duñach, M.; Seigneuret, M.; Riguad, J.-L.; Padrós, E. *J. Biol. Chem.* **1988**, *263*, 17378−17384.

(50) Mitra, A. K.; Stroud, R. M. *Biophys. J.* **1990**, *57*, 301−311.

(51) Sweetman, L. L.; El-Sayed, M. A. *FEBS Lett.* **1991**, *282*, 436–440.

(52) Jonas, R.; Ebrey, T. G. *Proc. Natl. Acad. Sci. U.S.A.* **1991**, *88*, 149–153.

(53) Zhang, N. Y.; El-Sayed, M. A. *Biochemistry* **1993**, *32*, 14173–14175.

(54) Zhang, Y. N.; Sweetman, L. L.; Awad, E. S.; El-Sayed, M. A. *Biophys. J.* **1992**, *61*, 1201–1206.

(55) Papadopoulos, G.; Dencher, N. A.; Zaccai, G.; Büldt, G. *J. Mol. Biol.* **1990**, *214*, 15–19.

(56) Ariki, M.; Lanyi, J. K. *J. Biol. Chem.* **1986**, *261*, 8167–8174.

(57) Ariki, M.; Magde, D.; Lanyi, J. K. *J. Biol. Chem.* **1987**, *262*, 4947–4951.

(58) Szundi, I.; Stoeckenius, W. *Proc. Natl. Acad. Sci. U.S.A.* **1987**, *84*, 3681–3684.

(59) Szundi, I.; Stoeckenius, W. *Biophys. J.* **1989**, *56*, 369–383.

(60) McIntosh, A. R.; Boucher, F. *Biophys. J.* **1991**, *60*, 1–7.

(61) Pierce, B. M. Personal communication.

(62) Sampogna, R. V.; Honig, B. *Biophys. J.* **1994**, *66*, 1341–1352.

(63) Govindjee, R.; Kono, M.; Balashov, S. P.; Imasheva, E.; Sheves, M.; Ebrey, T. G. *Biochemistry* **1995**, *34*, 4828–4838.

(64) Sonar, S.; Marti, T.; Rath, P.; Fischer, W.; Coleman, M.; Nilsson, A.; Khorana, H. G.; Rothschild, K. J. *J. Biol. Chem.* **1994**, *269*, 28851–28858.

(65) McDermott, A. E.; Thompson, L. K.; Winkel, C.; Farrar, M. R.; Pelletier, S.; Lugtenburg, J.; Herzfeld, J.; Griffin, R. G. *Biochemistry* **1991**, *30*, 8366–8371.

(66) Holz, M.; Drachev, L. A.; Mogi, T.; Otto, H.; Kaulen, A. D.; Heyn, M. P.; Skulachev, V. P.; Khorana, H. G. *Proc. Natl. Acad. Sci. U.S.A.* **1989**, *86*, 2167–2171.

(67) Otto, H.; Marti, T.; Holz, M.; Mogi, T.; Stern, L. J.; Engel, F.; Khorana, H. G.; Heyn, M. P. *Proc. Natl. Acad. Sci. U.S.A.* **1990**, *87*, 1018–1022.

(68) Butt, H. J.; Fendler, K.; Bamberg, E.; Tittor, J.; Oesterhelt, D. *EMBO J.* **1989**, *8*, 1657–1663.

(69) Fukumoto, J. M.; Hanamoto, J. H.; El-Sayed, M. A. *Photochem. Photobiol.* **1984**, *39*, 75–79.

(70) Gerwert, K.; Hess, B.; Engelhard, M. *FEBS Lett.* **1990**, *261*, 449–454.

(71) Jang, D.-J.; El-Sayed, M. A.; Stern, L. J.; Mogi, T.; Khorana, H. G. *Proc. Natl. Acad. Sci. U.S.A.* **1990**, *87*, 4103–4107.

(72) Rothschild, K. J.; Braiman, M. S.; He, Y.-W.; Marti, T.; Khorana, H. G. *J. Biol. Chem.* **1990**, *265 (28)*, 16985–16991.

(73) Dollinger, G.; Eisenstein, L.; Lin, S. L.; Nakanishi, K.; Termini, J. The role of tyrosine in the proton pump of bacteriorhodopsin. In *Biophysical studies of retinal proteins*; Ebrey, T. G., Frauenfelder, H., Honig, B., Nakanishi, K., Eds.; University of Illinois Press: 1987; pp 120–125.

(74) Dér, A.; Tóth-Boconádi, R.; Keszthelyi, L. *FEBS Lett.* **1988**, *229*, 313–316.

(75) Maeda, A.; Sasaki, J.; Yamazaki, Y.; Needleman, R.; Lanyi, J. K. *Biochemistry* **1994**, *33*, 1713–1717.

(76) Deng, H.; Huang, L.; Callender, R.; Ebrey, T. *Biophys. J.* **1994**, *66*, 1129–1136.

(77) Hildebrandt, P.; Stockburger, M. *Biochemistry* **1984**, *23*, 5539–5548.

(78) Harbison, G. S.; Roberts, J. E.; Herzfeld, J.; Griffin, R. G. *J. Am. Chem. Soc.* **1988**, *110*, 7221–7223.

(79) Nagle, J. F.; Morowitz, H. J. *Proc. Natl. Acad. Sci. U.S.A.* **1987**, *75*, 298–302.

(80) Cao, Y.; Varo, G.; Chang, M.; Ni, B.; Needleman, R.; Lanyi, J. K. *Biochemistry* **1991**, *30*, 10972–10979.

(81) Brown, L. S.; Varo, G.; Hatanaka, M.; Sasaki, J.; Kandori, H.; Maeda, A.; Friedman, N.; Sheves, M.; Needleman, R.; Lanyi, J. K. *Biochemistry* **1995**, *34*, 12903–12911.

(82) Jang, D. J.; Corcoran, T. C.; El-Sayed, M. A. *Photochem. Photobiol.* **1988**, *48*, 209–217.

(83) Drachev, L. A.; Kaulen, A. D.; Khitrina, L. V. *Biokhimiya* **1988**, *53*, 663–667 (in Russian).

(84) Druzhko, A. B.; Zharmukhamedov, S. K. Biochrome film based on some analogues of bacteriorhodopsin. In *Photosensitive biological complexes and optical recording of information*; Ivanitskiy, G. R., Vsevolodov, N. N., Eds.; USSR Academy of Sciences: Biological Research Center, Institute of Biological Physics, Pushchino, 1985; pp 119–125.

(85) Savranskiy, V. V.; Tkachenko, N. V.; Chukharev, V. I. Kinetics of diffraction effectiveness of bacteriorhodopsin. In *Photosensitive biological complexes and optical recording of information*; Ivanitskiy, G. R., Vsevolodov, N. N., Eds.; USSR Academy of Sciences: Biological Research Center, Institute of Biological Physics, Pushchino, 1985; pp 97–100.

(86) Vsevolodov, N. N.; Poltoratskii, V. A. *Sov. Phys. Tech. Phys.* **1985**, *30*, 1235.

(87) Jonas, R.; Koutalos, Y.; Ebrey, T. G. *Photochem. Photobiol.* **1990**, *52*, 1163–1177.

(88) Tan, E. H. L.; Govender, D. S. K.; Birge, R. R. *J. Am. Chem. Soc.* **1996**, *110*, 2752–2753.

(89) Varo, G.; Lanyi, J. K. *Biochem.* **1991**, *30*, 7165–7171.